ELSEVIER

Contents lists available at ScienceDirect

Composites Part B

journal homepage: www.elsevier.com/locate/compositesb



N/S co-doped nanocomposite of graphene oxide and graphene-like organic molecules as all-carbonaceous anode material for high-performance Li-ion batteries

Wooree Jang ^{a,b}, Jongmin Kim ^c, Seoyun Lee ^{a,d}, Seokhoon Ahn ^{a,e}, Hyeyoung Koo ^{a,**}, Cheol-Min Yang ^{a,e,*}

ARTICLE INFO

Handling Editor: Prof. Joong Lee

Keywords:
Li-ion battery
Graphene oxide
Graphene-like organic molecules
N/S co-doping
All carbonaceous anode

ABSTRACT

In this study, to enhance the electrochemical performance of graphene-based anodes for Li-ion batteries (LIBs), we synthesized an all-carbonaceous N/S co-doped nanocomposite of graphene oxide (GO) and graphene-like small organic molecules (GOM) using a mild, eco-friendly, one-step hydrothermal method with thiourea (CH₄N₂S) (denoted as h-N/S-GO/GOM). The thiourea facilitated N/S co-doping and $\pi-\pi$ bonding, which improved the interaction between hydrophilic GO and hydrophobic GOM in aqueous solution. Notably, the formation of π - π bonds between GO and GOM created pathways that enhanced electron transfer, thereby promoting efficient Li-ion transport from the electrolyte through the channels during rapid charge-discharge cycles. Additionally, the functional groups resulting from N/S co-doping increased the number of active sites within the nanocomposite. Consequently, the h-N/S-GO/GOM anode demonstrated superior electrochemical performance, achieving an average reversible capacity of 1265 mAh g⁻¹ at 0.1 A g⁻¹ and retaining 83.0 % of its capacity after 200 cycles. Furthermore, the nanocomposite exhibited excellent long-term cycling stability, maintaining a capacity of 688 mAh g⁻¹ even after 1000 cycles at a high current density of 1.0 A g⁻¹. The hierarchical network structure of the all-carbonaceous h-N/S-GO/GOM anode facilitated efficient charge transfer between the electrode and electrolyte through shorter diffusion paths for Li-ion transport and provided additional active sites, contributing to its outstanding electrical performance. The h-N/S-GO/GOM nanocomposite represents a promising alternative to traditional graphite-based anodes, offering a path toward highperformance, eco-friendly LIBs suitable for applications such as electric vehicles and energy storage systems.

1. Introduction

Recently, the demand for Li-ion batteries (LIBs) has been on the rise owing to their widespread use in portable power devices and various transportation applications, including electric vehicles (EVs), hybrid EVs, and plug-in hybrid EVs [1]. As large-scale industries such as EVs and energy storage systems (ESSs) experience substantial growth, considerable attention has been directed toward developing environmentally friendly and cost-effective electrode materials with high

energy and power densities within a limited electrode area [2,3]. Graphite, a carbon material with a stacked two-dimensional (2D) layered structure, has garnered significant interest in LIB anode research due to its high reversible capacity based on intercalation and de-intercalation processes and excellent cycle stability. However, graphite has a relatively low theoretical capacity (372 mA h g⁻¹), which is insufficient to meet the requirements of large-scale applications for high energy densities [4–6]. Graphene, with its 2D monolayer structure, is expected to be a promising alternative to graphite as an anode

E-mail addresses: koohy@kist.re.kr (H. Koo), cmyang1119@kist.re.kr (C.-M. Yang).

https://doi.org/10.1016/j.compositesb.2024.111994

Received 6 August 2024; Received in revised form 11 November 2024; Accepted 18 November 2024 Available online 20 November 2024

1359-8368/© 2024 The Authors. Published by Elsevier Ltd. This is an open access article under the CC BY-NC-ND license (http://creativecommons.org/licenses/by-nc-nd/4.0/).

a Institute of Advanced Composite Materials, Korea Institute of Science and Technology (KIST), Wanju-gun, Jeonbuk State, 55324, Republic of Korea

b Defense and Safety Protection Materials, Korea Institute of Convergence Textile (KICTEX), Iksan-si, Jeonbuk State, 54588, Republic of Korea

^c Division of Energy Technology, DGIST, Daegu, 42988, Republic of Korea

^d Department of Energy Science, Sungkyunkwan University (SKKU), Suwon, 16419, Republic of Korea

e Department of JBNU-KIST Industry-Academia Convergence Research, Jeonbuk National University, Jeonbuk State, 54896, Republic of Korea

^{*} Corresponding author. Institute of Advanced Composite Materials, Korea Institute of Science and Technology (KIST), Wanju-gun, Jeonbuk State, 55324, Republic of Korea.

^{**} Corresponding author.

material, offering high energy and power densities due to its good chemical stability, excellent electronic transport properties, high specific surface area (SSA), and flexibility. Despite the superior electrochemical properties of graphene, challenges such as low rate capability, large voltage hysteresis, and the potential risk of Li dendrite growth remain [1,6-8]. To address these issues, graphene derivatives such as graphene oxide (GO), reduced GO (rGO), N-doped rGO, and GO-based composites have been extensively investigated. These approaches include: 1) introducing spacers between graphene nanosheets to mitigate restacking and enhance SSA, 2) constructing three-dimensional (3D) architectures and introducing pores into the graphene-based structure to facilitate ion transport, and 3) doping with heteroatoms and functionalizing with metal oxides or conducting polymers to amplify capacitance [9–15]. These derivatives exhibit key attributes such as porous structures with high SSA and rapid electron transport, contributing to short Li-ion diffusion distances. These features make graphene-based composites desirable for high energy and power densities, enhancing the rate capability by enabling faster kinetics at the electrode/electrolyte interfaces.

Among graphene derivatives, small organic molecular electrodes fabricated using redox-active processes with environmentally friendly chemical compositions, such as C, O, N, and H, have gained significant attention as promising candidates for LIBs due to their eco-friendly, sustainable, and inexpensive properties, as well as their unique flexible structures [16-18]. However, these small organic molecules tend to dissolve in non-aqueous electrolytes, leading to a sharp decrease in their electrochemical capacity due to low electrical conductivity and poor cycling stability [5,19]. Recently, Park et al. reported the use of contorted polycyclic aromatic hydrocarbon molecules, such as contorted hexabenzocoronene (c-HBC), in LIB anode materials [5]. The c-HBC crystal was transformed into a new polymorph through specific solvent and thermal annealing treatments, achieving capacities of 265 mAh g⁻¹. Additionally, they found that c-HBC facilitated easy access of Li-ions to the anode materials through nanopore channels, resulting in excellent storage stability. In this study, we selected graphene-like small organic molecules (GOM) for their unique properties that enhance the electrochemical performance of GO-based anodes in LIBs. Similar to c-HBC, GOM are twisted polycyclic aromatic hydrocarbons known to form molecular wires through π - π interactions, greatly improving charge transport efficiency. This structure supports rapid electron mobility, which is essential for efficient charge-discharge cycles in energy storage. Previous studies have shown that this structure creates nanopore channels, enhancing Li-ion access and storage stability during cycling [5]. Furthermore, the conjugated aromatic structure of GOM prevents electrolyte dissolution, a common issue with other organic molecules, thus supporting long-term cycling stability. GOM can also be doped with heteroatoms, such as F, which enhances Li-ion accessibility, rate performance, and long-term stability [20]. This doped structure improves both conductivity and ion diffusion, providing GOM with a distinct advantage over other organic electrode materials. Unlike other organic molecules, such as conducting polymers, which may offer high electronic properties but often suffer from poor cycling stability due to electrolyte solubility, GOM provide an optimal combination of high conductivity, structural stability, and chemical flexibility through doping [21]. The π -conjugated structures and heteroatom doping potential make GOM promising candidates as high-rate-performance and stable structures in LIB applications.

In this study, we propose a new synergistic GO-based nanocomposite anode material combined with organic molecules to address issues such as the dissolution of organic molecules and the insufficient electrochemical performance of graphene-based materials. Notably, the organic molecules, which feature 13 benzene rings similar to the graphene structure, act as spacers between the graphene nanosheets, effectively promoting charge transfer via $\pi-\pi$ stacking within the nanocomposite [5,21]. Moreover, utilizing thiourea (CH₄N₂S), known for its strong binding affinity between compounds, enhances the

bonding strength between GO and organic molecules while improving the electrochemical performance of graphene-based nanocomposites by generating active sites through heteroatom co-doping of N and S. Several studies have demonstrated that co-doping with two highly interacting heteroatoms (N and S) in a carbon matrix can induce a synergistic effect to enhance electrochemical performance [10,22–25]. Doping graphene with heteroatoms (B, N, F, S, or P) disrupts its inert structure, enhancing its specific capacity and rate performance. N/S co-doping is particularly effective, as N introduces free electrons and S creates defects that promote electron transport through π – π interactions, improving charge mobility and generating more active sites for Li electroactivity [26,27]. Recent studies, such as that by Ren et al., have shown that co-doping with multiple heteroatoms further boosts conductivity and electrochemical performance, making it a powerful strategy for optimizing graphene-based electrodes [10,21–25,28].

Therefore, we report a nanocomposite comprising N/S co-doped GO and GOM as an all-carbonaceous LIB anode material. The N/S co-doped GO/GOM nanocomposite was prepared via a facile hydrothermal method under eco-friendly and mild conditions. Notably, this all-carbonaceous nanocomposite, composed solely of graphene derivative materials, demonstrated significantly superior electrochemical performance, with an average reversible capacity of $1265\,\mathrm{mAh\,g^{-1}}$ at $0.1\,\mathrm{A\,g^{-1}}$ and retained 83.0 % of its capacity after 200 cycles. These results highlight enhanced electrochemical performance within a constrained anode area, attributed to the synergistic effects of fast charge transfer through cross-linked networks, active chemical reactions due to codoping, and the formation of nanopores via GOM. This provides promising prospects for carbon material electrodes in high-energy/power LIBs.

2. Materials and methods

2.1. Preparation of GO-based nanocomposites

GO (average lateral size of 3–4 μ m, Grapheneall Co., Ltd., Korea) and thiourea powder (ACS reagent, 99.0 %, Sigma-Aldrich, Germany) were purchased from their respective suppliers. GOM were prepared as previously reported: synthesized by reacting 6,13-pentacenequinone ($C_{22}H_{12}O_2$) with tetrabromomethane (CBr₄) and triphenylphosphine (P(C₆H₅)₃), followed by a reaction with phenylboronic acid (C₆H₅B (OH)₂), tripotassium phosphate (K₃PO₄), and a palladium catalyst. Following purification, the product underwent cyclization with iodine (I₂) and propylene oxide (C₃H₆O) under UV light, followed by a second cyclization with iron chloride (FeCl₃) and nitromethane (CH₃NO₂), and a final purification [5]. All reagents used for the preparation of GOM were purchased from Sigma-Aldrich (Germany).

The N/S co-doped GO/GOM nanocomposite was prepared using a hydrothermal method. GO (50 mg) was first dispersed in deionized (DI) water (50 mL) via bath sonication for 2 h. GOM (12.5 mg) were then added to the GO solution and sonicated for 1 h. Thiourea powder (200 mg) was subsequently mixed with the GO/GOM solution and sonicated for 2 h. The mixed solution was transferred to a Teflon-lined stainless-steel autoclave, sealed, and maintained at 150 °C for 4 h. The resulting black nanocomposite was rinsed with DI water and ethanol, and centrifuged at 8000 rpm for 10 min. This rinsing step was repeated thrice to remove any residual ions. After centrifugation and freezedrying, an N/S co-doped GO/GOM nanocomposite was successfully obtained (h-N/S-GO/GOM).

To elucidate the role of thiourea in the *h*-N/S-GO/GOM nanocomposite, three types of nanocomposites (GO and GOM, with and without hydrothermal treatment) were prepared using equal quantities of GO, GOM, thiourea powder, and DI water as follows: (a) a nanocomposite of GO and GOM was obtained by mixing GO and GOM in DI water and freeze-drying without hydrothermal treatment (*m*-GO/GOM); (b) a hydrothermal reaction was performed on a mixture of GO and GOM in DI water without adding thiourea under the same conditions as for *h*-

N/S-GO/GOM (h-GO/GOM); and (c) to investigate the effect of GOM on the electrochemical performance of the h-N/S-GO/GOM nanocomposite, N/S co-doped GO was prepared using a hydrothermal process without GOM under the same conditions (h-N/S-GO).

2.2. Characterization

The surface chemical structures were confirmed using X-ray photoelectron spectroscopy (XPS; K-Alpha, Thermo Fisher Scientific, USA). The crystalline structures were analyzed with X-ray diffraction (XRD; Rigaku SmartLab, Japan) using Cu-K_{α} radiation ($\lambda = 0.154$ nm) over a 2θ range of 5°-80°. Structural properties were characterized by Raman spectroscopy with an excitation laser wavelength of 514 nm (Horiba, Japan). Morphologies and elemental distributions were investigated using field-emission scanning electron microscopy (FESEM) with energy-dispersive X-ray spectroscopy (EDS; Verios 460L, FEI, USA) and high-resolution transmission electron microscopy (HRTEM; Tecnai G2 F20, FEI, USA) at 200 kV. SSAs were evaluated using N2 adsorption/ desorption isotherms measured at 77 K with volumetric adsorption equipment (BELSORP-max, MicrotracBEL, Japan), following preevacuation to a base pressure of 10⁻⁴ Pa at 150 °C for 2 h and applying the Brunauer-Emmett-Teller (BET) method. Electrical conductivities were estimated as functions of pressure using a powder resistivity measurement system (HPRM-M2, Hantech, Korea). The powder samples were compressed in a cylindrical mold with an area of 3.8 cm² at room temperature.

2.3. LIB assembly and electrochemical measurements

LIB anode slurries were prepared by homogeneously mixing 80 wt% h-N/S-GO/GOM or comparative samples (active material), 15 wt% Super-P (conductive agent), and 5 wt% polyvinylidene fluoride (binder) in N-methyl-2-pyrrolidone (NMP; C_5H_9NO). The slurries were then coated onto Cu foil and dried in a vacuum oven at 80 °C for 12 h to evaporate the NMP solvent. After drying, the films were cut into discs of diameter 15 mm and used as anodes. The loading of active materials was approximately 0.45 mg cm $^{-2}$. The anodes were assembled into 2032-type coin cells with Li metal as the counter/reference electrodes, a porous polyethylene membrane as the separator, and a mixed solution of 1 M Li hexafluorophosphate (LiPF₆) dissolved in ethylene carbonate ($C_3H_4O_3$)/dimethyl carbonate ((CH_3O_2CO) (1:1 in volume) as the electrolyte, all within an Ar-filled glove box. The electrochemical performance of the h-N/S-GO/GOM and comparative samples was

measured using a battery test system (WBCS3000, Won-A Tech, Korea). Cyclic voltammetry (CV) measurements were conducted over a potential window of 0.005–3.0 V vs. Li/Li⁺ at various scan rates. Galvanostatic charge/discharge (GCD) measurements were performed at different current densities. Electrochemical impedance spectroscopy (EIS) measurements were conducted in the frequency range of 100 kHz to 10 MHz using an electrochemical workstation (ZIVE SP2, Won-A Tech, Korea).

3. Results and discussion

Fig. 1 illustrates the preparation process of a 2D graphene-based nanocomposite comprising GO and GOM, denoted as h-N/S-GO/GOM. This nanocomposite was synthesized using a hydrothermal method for N/S co-doping with thiourea. The addition of thiourea improved the miscibility of GO and GOM in DI water, enhancing network formation and N/S co-doping effects [29,30]. The resulting cross-linked structures, combined with the π -electron-conjugated GOM, facilitated effective electron transfer. The h-N/S-GO/GOM nanocomposite, with its conjugated network and N/S co-doping, provided multiple pathways for efficient Li-ion transport through $\pi-\pi$ interactions and robust chemical reactions. Consequently, the structural synergy of the h-N/S-GO/GOM nanocomposite enhanced its electrical conductivity, resulting in superior electrochemical performance. For comparison, we also prepared m-GO/GOM, h-GO/GOM, and h-N/S-GO using simple solution mixing or hydrothermal methods, with or without thiourea, to examine the impact of thiourea and GOM incorporation on their electrochemical properties.

The morphology and microstructure of the h-N/S-GO/GOM nanocomposite were analyzed using FESEM and HRTEM, and compared with *m*-GO/GOM and *h*-GO/GOM (Fig. 2). Unlike the pristine GO nanosheets, which exhibit ripples and wrinkles (Figs. S1a and b), the m-GO/GOM nanocomposite displayed a morphology influenced by GOM incorporation, with GOM agglomerating at the edges of the GO nanosheets due to the poor dispersibility of hydrophobic GOM in aqueous solution (Fig. 2a and d). In contrast, the h-GO/GOM nanocomposite, synthesized without thiourea via hydrothermal processing, presented a more crumpled and contracted morphology compared to m-GO/GOM, owing to the reduction of GO nanosheets during the hydrothermal process (Fig. 2b and e), with aggregated GOM positioned between the wrinkles. In comparison, the h-N/S-GO/GOM nanocomposite exhibited a uniform distribution of GOM on the GO nanosheets, differing from *m*-GO/GOM and *h*-GO/GOM. Notably, the h-N/S-GO/GOM nanocomposite features a cross-linked honeycomb structure with pores of varying sizes, presenting a promising design for efficient Li-ion transport through π - π interactions and

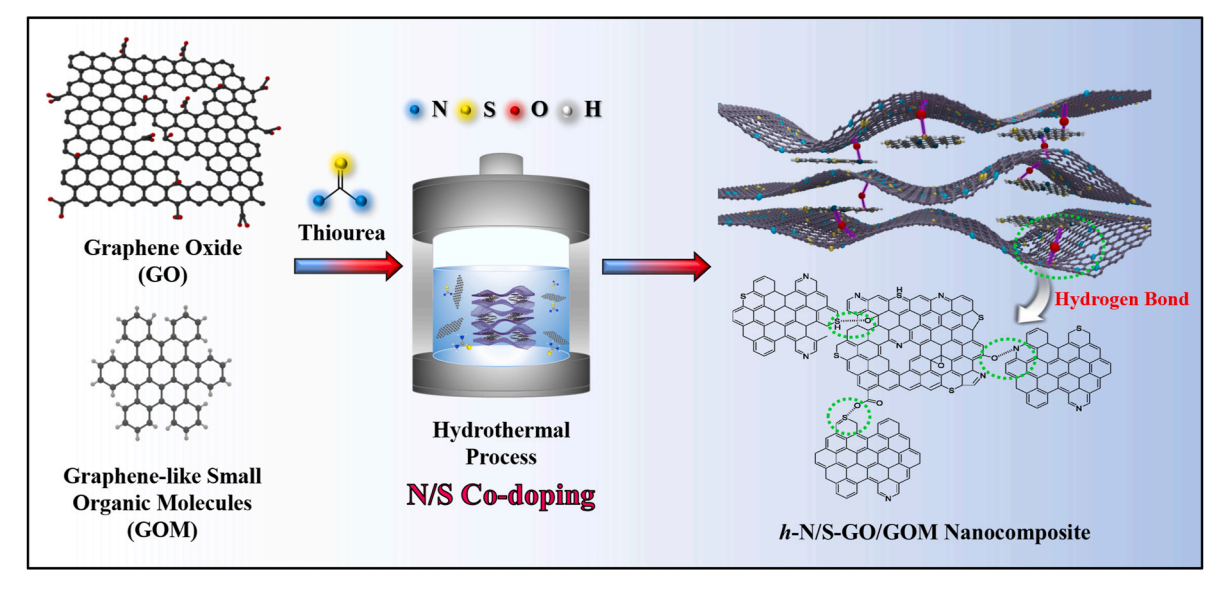


Fig. 1. Schematic of the h-N/S-GO/GOM nanocomposite preparation process.

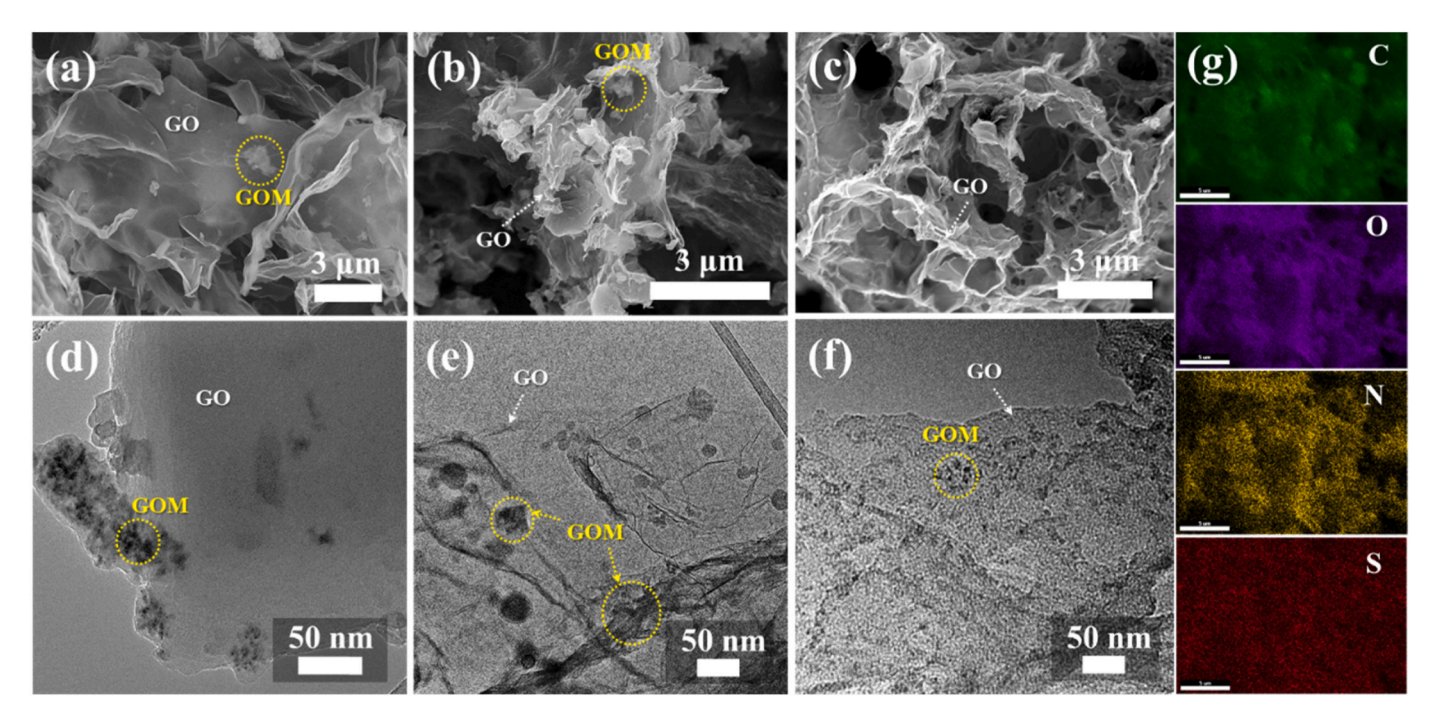


Fig. 2. FESEM and HRTEM images of (a, d) *m*-GO/GOM, (b, e) *h*-GO/GOM, and (c, f) *h*-N/S-GO/GOM nanocomposites, and (g) EDS elemental mapping images of the *h*-N/S-GO/GOM nanocomposite.

active chemical reactions. These morphological improvements are attributed to the enhanced miscibility and chemical bonding between GO nanosheets and GOM facilitated by thiourea (Fig. 2c and f) [30–32]. Moreover, EDS elemental mapping confirmed that in the h-N/S-GO/GOM nanocomposite, thiourea provided N and S, resulting in a uniform distribution of C, O, N, and S throughout the graphene-based structure (Fig. 2g).

To investigate the chemical bonding in the *h*-N/S-GO/GOM nano-composite resulting from N/S co-doping with thiourea, XPS analysis was

performed on h-N/S-GO/GOM and comparative samples (Fig. 3). The XPS survey revealed atomic ratios of C to O (C/O) of 1.98, 11.82, 2.17, 5.17, and 7.37 for GO, GOM, m-GO/GOM, h-GO/GOM, and h-N/S-GO/GOM, respectively (Fig. 3a—c, Figs. S2a and b, Table 1). The C content in the nanocomposites increased with the incorporation of GOM, while the O-containing functional groups in the GO nanosheets were partially removed through partial reduction during the hydrothermal process. Consequently, the h-N/S-GO/GOM nanocomposite exhibited the highest C/O ratio, serving as a reliable indicator of the high quality of the

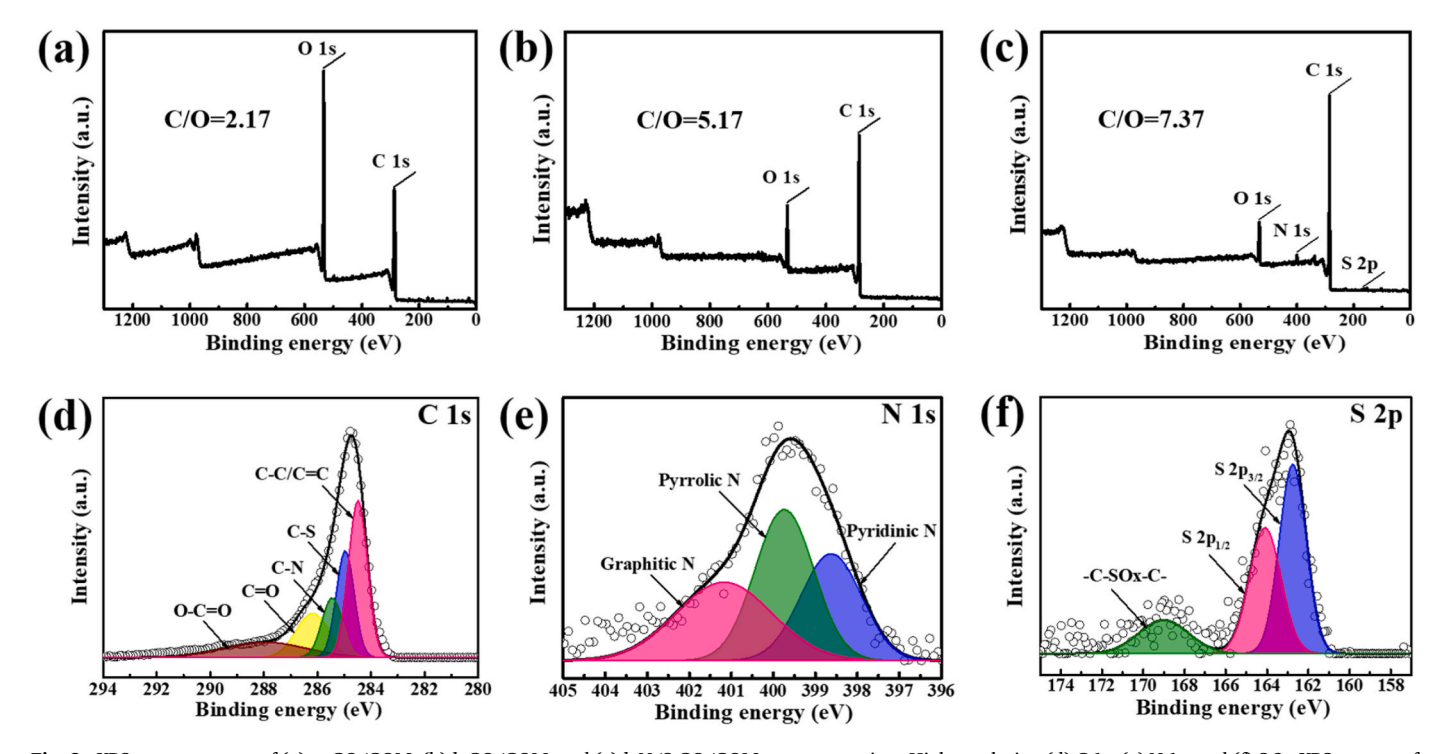


Fig. 3. XPS survey spectra of (a) *m*-GO/GOM, (b) *h*-GO/GOM, and (c) *h*-N/S-GO/GOM nanocomposites. High-resolution (d) C 1s, (e) N 1s, and (f) S 2p XPS spectra of the *h*-N/S-GO/GOM nanocomposite.

graphene-based nanocomposite. The presence of N (2.5 at%) and S (0.5 at%), along with C (85.5 at%) and O (11.6 at%), in the h-N/S-GO/GOM nanocomposite was confirmed (Table 1), validating the successful N/S co-doping with thiourea.

The C 1s spectrum of the h-N/S-GO/GOM nanocomposite revealed peaks at 284.5, 285.0, 285.5, 286.2, and 288.2 eV, corresponding to the C–C/C=C, C–S, C–N, C=O, and O–C=O functional groups, respectively (Fig. 3d) [33]. The deconvoluted N 1s spectrum showed peaks at 398.6, 399.7, and 401.2 eV, representing pyridinic, pyrrolic, and graphitic N, respectively (Fig. 3e) [25]. Additionally, the S 2p spectrum displayed peaks at 162.8 and 164.1 eV for S $2p_{3/2}$ and S $2p_{1/2}$ in C–S bonding, respectively, and a peak at 169.0 eV corresponding to S atoms bonded with O atoms (Fig. 3f) [25,34,35]. These results indicate that S atoms formed chemical bonds with O atoms in the GO nanosheets. Overall, the XPS analysis demonstrated that the h-N/S-GO/GOM nanocomposite was effectively synthesized, exhibiting the formation of chemical bonds, including hydrogen and conjugated bonds, as a result of N/S co-doping.

The XRD pattern of the h-N/S-GO/GOM nanocomposite was compared with those of GO, GOM, m-GO/GOM, and h-GO/GOM (Fig. 4a). The XRD pattern of the h-N/S-GO/GOM nanocomposite exhibited a broad peak at 20-30° and a smaller peak near 43°, corresponding to the (002) and (100) planes of multilayer graphene, respectively [36]. Additionally, four distinct peaks at 9.8°, 18.7°, 23.0°, and 26.3° were attributed to the (101), (003), (113), and (104) planes, respectively, due to the GOM component [5]. The observed narrowing and shifting of the characteristic graphite diffraction peak from 24.5° to 24.7° indicate a reduction in the interlayer distance of the stacked graphene sheets. The interlayer d-spacing of the h-N/S-GO/GOM nanocomposite (0.35 nm) was significantly smaller than that of the GO nanosheets (0.75 nm) and the m-GO/GOM nanocomposite (0.79 nm), suggesting that O-containing functional groups were partially removed from the GO nanosheets owing to the partial reduction of GO nanosheets during the hydrothermal process for N/S co-doping (Table 1) [37]. To illustrate this reduction effect, we have included the C 1s XPS spectra of m-GO/GOM and h-GO/GOM (Fig. S3) [38]. Furthermore, the interlayer d-spacing of the h-N/S-GO/GOM nanocomposite was slightly smaller than that of h-GO/GOM, due to the denser structure and chemical bonding between the distributed GOM and GO nanosheets, contrasting with the h-GO/GOM nanocomposite which exhibited poorer dispersibility [39]. The N₂ adsorption isotherms for GO, GOM, m-GO/GOM, h-GO/GOM, and h-N/S-GO/GOM are shown in Fig. S4. The N₂ adsorption isotherm of the h-N/S-GO/GOM nanocomposite exhibited an intermediate shape between types II and IV, with a pronounced hysteresis loop at high P/P_0 . The BET SSA of the h-N/S-GO/GOM nanocomposite was calculated to be 68 m² g⁻¹, notably lower than that of the h-GO/GOM nanocomposite (113 m² g⁻¹) (Table 1). This decrease is consistent with the reduction in interlayer spacing observed in the XRD results, indicating that the chemical bonding between GOM and GO nanosheets contributes to this effect (Table 1). In graphene materials, XRD peak positions are influenced by interlayer d-spacing, while peak width is largely determined by the size of graphitic domains, which are separated laterally by grain boundaries and longitudinally by sp²/sp³ domain boundaries. The crystallite size (D), representing the vertical dimension of maintained graphitic ordering, can be calculated using the Debye-Scherrer formula [36,40]:

$$D = \frac{k\lambda}{\beta\cos\theta} \tag{1}$$

where k represents Scherrer's constant, β is the full-width at half maximum (FWHM), λ denotes the wavelength of the radiation, and θ signifies Bragg's angle. Here, k is a constant related to the crystallite shape, typically assumed to be 0.89 for a spherical crystal with a cubic unit cell. The values calculated for the samples are presented in Table 1. The D values tended to increase in the presence of GOM (similar to the graphene structure). In particular, synergistic interfacial interactions, such as hydrogen bonding, electrostatic attraction, and π - π stacking inside the h-N/S-GO/GOM nanocomposite, can enhance the crystallite size [41]. As the crystallite size increases, the free path of carriers increases and the diffusion distance of Li-ions decreases, thereby enhancing electrical conductivity [42,43].

Raman analysis was performed to further verify the structure and quality of the graphene-based composites, as shown in Fig. 4b. Two prominent peaks at approximately 1350 cm⁻¹ (D-band) and 1590 cm⁻¹ (G-band) were observed, associated with disordered and graphitic structures, respectively (Table S1). In the h-N/S-GO/GOM nanocomposite, the *G*-band displayed a red shift to 1583.10 cm⁻¹ compared to the other samples, indicating structural distortions that tighten the sp² carbon network and increase vibrational frequency through π - π interactions between adjacent layers or within the nanocomposite. Additionally, doping elements such as N and S modify the electron density and create defects, further contributing to this shift. The combined effects of doping and π - π interactions strengthen the carbon structure, enhancing both rigidity and charge migration [44,45]. Moreover, the I_D/I_G ratio (i.e., the integrated intensity ratio between the D- and G-bands) is a crucial parameter for determining the degree of defects in the carbon structure. The h-N/S-GO/GOM nanocomposite exhibited the highest I_D/I_G ratio of 1.72, indicating increased defect concentration due to the introduction of small-sized GOM and chemical doping, compared to GO, m-GO/GOM, and h-GO/GOM [46,47].

To assess the beneficial effects of N/S co-doping in graphene-based nanocomposites as LIB anodes, the electrochemical properties of the h-N/S-GO/GOM and comparative (GO, GOM, m-GO/GOM, and h-GO/GOM) anodes were investigated in a coin-type half-cell configuration. Fig. 5a illustrates the CV curves of the h-N/S-GO/GOM nanocomposite at a scan rate of 0.1 mV s $^{-1}$. During the first discharge cycle, two cathodic plateaus were observed at approximately 1.60 and 0.65 V, which disappear in subsequent cycles. These results are attributed to the formation of a solid–electrolyte interface (SEI) film, an irreversible side reaction associated with electrolyte decomposition [25,48]. The CV curves exhibited good overlap without significant changes after the initial scan, indicating the structural stability of the h-N/S-GO/GOM nanocomposite during subsequent cycles due to its densely connected networks with chemical bonding.

The charge and discharge curves of the h-N/S-GO/GOM nanocomposite were examined at a current density of $0.1~{\rm A~g}^{-1}$ in the voltage range 0.05– $3.00~{\rm V}$ (Fig. 5b). Two plateaus at approximately 1.60 and $0.65~{\rm V}$ were observed during the first discharge process, signifying SEI layer formation and electrolyte decomposition, consistent with the CV

Table 1

XPS, XRD, and BET SSA analyses of the h-N/S-GO/GOM nanocomposite and comparative samples (GO, GOM, m-GO/GOM, and h-GO/GOM).

Samples	XPS (at%)					XRD				N ₂ adsorption
	С	N	О	S	C/O	2θ	FWHM	Interlayer d-spacing (d, nm)	Crystallite size (D, nm)	BET SSA (m ² g ⁻¹)
GO	66.4	0.0	33.6	0.0	1.98	11.75	1.50	0.75	5.27	12
GOM	92.2	0.0	7.8	0.0	11.82	18.50	0.40	0.48	19.91	7
m-GO/GOM	68.4	0.0	31.6	0.0	2.17	11.15	1.90	0.79	4.15	57
h-GO/GOM	83.8	0.0	16.2	0.0	5.17	24.60	13.83	0.36	0.58	113
h-N/S-GO/GOM	85.5	2.5	11.6	0.5	7.37	24.83	13.00	0.35	0.62	68

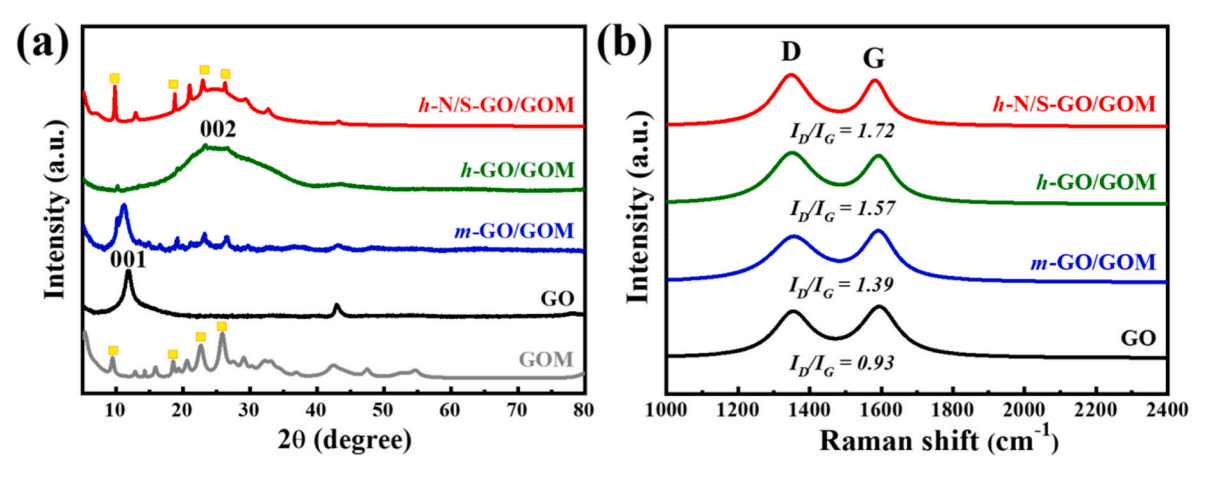


Fig. 4. (a) XRD patterns and (b) Raman spectra of the h-N/S-GO/GOM nanocomposite and comparative samples (GO, GOM, m-GO/GOM, and h-GO/GOM).

results. The first discharge and charge capacities of the h-N/S-GO/GOM nanocomposite anode were 2036 and 1104 mAh g⁻¹, respectively, resulting in a Coulombic efficiency of 54.2 %. This initial low Coulombic efficiency can be attributed to the formation of SEI layers on the surface of the electrode material, involving electrolyte decomposition and irreversible Li-ion insertion into the active materials. This process is particularly prevalent in the early cycles, resulting in an initial loss of Liions [49]. Additionally, the relatively low initial Coulombic efficiency of the h-N/S-GO/GOM nanocomposite anode can be attributed to the passivation of highly active carbon atoms due to N/S co-doping. While this doping strategy enhances reversibility and reduces irreversible surface reactions between graphene and the electrolyte, Li-ion consumption still occurs due to SEI formation during the initial cycles. However, the passivation effect from N/S co-doping helps to suppress further irreversible reactions, minimizing Li-ion consumption and improving overall electrochemical performance in subsequent cycles [50]. Notably, the Coulombic efficiency of the h-N/S-GO/GOM nanocomposite anode gradually increased in subsequent cycles and stabilized at over 95.0 % after 10 cycles, demonstrating the effectiveness of N/S co-doping in enhancing the long-term cycling stability and efficiency of the anode material.

Fig. 5c illustrates the rate performance of the h-N/S-GO/GOM and comparative (GO, GOM, m-GO/GOM, and h-GO/GOM) anodes, evaluated at various current densities ranging from 0.1 to 10.0 A g⁻¹. The average reversible capacities are summarized in Table S2. The h-N/S-GO/GOM anode exhibited average reversible capacities of 1265, 976, 763, 619, 495, 340, and 221 mAh g^{-1} at current densities of 0.1, 0.2, 0.5, 1.0, 2.0, 5.0, and 10.0 A g⁻¹, respectively. Fig. S5 illustrates the consistent rate performance of h-N/S-GO/GOM, with error bars from multiple measurements confirming the reproducibility and reliability of the results despite minor fluctuations [19,51]. These capacities were significantly higher than those of GO, GOM, m-GO/GOM, and h-GO/GOM. This enhancement is attributed to the cross-linked structure with N/S co-doping, which facilitates rapid charge transfer and active chemical reactions, thereby improving electrochemical performance. In contrast, m-GO/GOM and h-GO/GOM exhibited poor charge mobility due to immiscible interfacial interactions between hydrophilic GO nanosheets and hydrophobic GOM, leading to lower electrical conductivity and inferior electrochemical performance [52]. Furthermore, the GO anode showed a higher initial reversible capacity compared to m-GO/GOM and h-GO/GOM anodes due to the presence of abundant O-containing functional groups, such as -COOH and -OH, which can store more Li-ions [53]. The GOM anode exhibited poor electrochemical performance due to insufficient electrical conductivity, although it exhibited better cycling stability than other anodes due to its conjugated structure and good chemical stability (Fig. S6) [54]. Notably, when the current density decreased from 10 to 0.1 A g⁻¹ after 70 cycles, the

reversible capacity of the h-N/S-GO/GOM anode recovered to 1038 mAh g^{-1} , retaining approximately 82.0 % of its initial capacity (Fig. 5d). This indicates excellent stability of the nanocomposite at high current charge and discharge rates. For comparative anodes (GO, GOM, m-GO/GOM, and h-GO/GOM), capacity retention rates when the current density returned from 10.0 to 0.1 A g⁻¹ were 52.6 %, 89.8 %, 63.9 %, and 85.6 %, respectively (Fig. 5d). The h-N/S-GO/GOM and h-GO/GOM anodes exhibited relatively stable electrochemical performances even after 70 cycles. This remarkable stability is attributed to their C=C conjugated structure, which imparts superior rate capability and cycling stability [55]. Previous research by Zhengwei et al. reported that the C=C bond is crucial for rate performance and stability, while O-containing functional groups improve reversible charge capacity [56]. Therefore, the relatively lower content of O-containing bonds in h-N/S-GO/GOM compared to h-GO/GOM contributes to its enhanced rate performance and stability.

Additionally, we compared the rate performance of the h-N/S-GO anode with that of the GO and h-N/S-GO/GOM anodes at various current densities ranging from 0.1 to 10.0 A g⁻¹ to evaluate the effect of GOM incorporation on electrochemical performance (Fig. S7). The average reversible capacities of the h-N/S-GO anode were 587, 416, 338, 287, 240, 177, and 127 mAh g⁻¹ at current densities of 0.1, 0.2, 0.5, 1.0, 2.0, 5.0, and 10.0 A g⁻¹, respectively, which were significantly lower than those of the h-N/S-GO/GOM anode. The hydrothermal treatment with GOM enhanced π - π interactions and introduced additional bonding mechanisms, such as hydrogen bonding. These interactions improve charge transfer pathways and strengthen the structural integrity, thereby boosting the rate performance of the h-N/S-GO/GOM anode compared to the h-N/S-GO anode. GO initially exhibited a higher capacity due to O-containing functional groups contributing to surface charge storage. However, its capacity sharply decreased at higher current densities because of limited surface storage. In contrast, the h-N/S-GO anode retained a higher capacity at elevated current densities, benefiting from improved conductivity and ion diffusion provided by N/ S co-doping and the partial reduction of GO. When the current density was decreased from 10.0 to 0.1 A $\rm g^{-1}$ after 70 cycles, the h-N/S-GO anode retained a reversible capacity of 535 mAh g^{-1} (91.2 %). However, the h-N/S-GO anode exhibited unstable reversible capacity after 70 cycles, likely due to the presence of functional groups introduced through N/S co-doping.

The cyclic stability of the h-N/S-GO/GOM anode was evaluated for 200 cycles at a current density of 0.1 A g $^{-1}$ (Fig. 5e). The introduction of GOM and N/S co-doping into GO nanosheets enhances electrolyte ion accessibility and facilitates efficient Li-ion transport during rapid charge–discharge processes. Consequently, the h-N/S-GO/GOM anode exhibited a higher reversible capacity of 1050 mAh g $^{-1}$ (83.0 %) after 200 cycles, surpassing the capacities of GO (358 mAh g $^{-1}$), m-GO/GOM

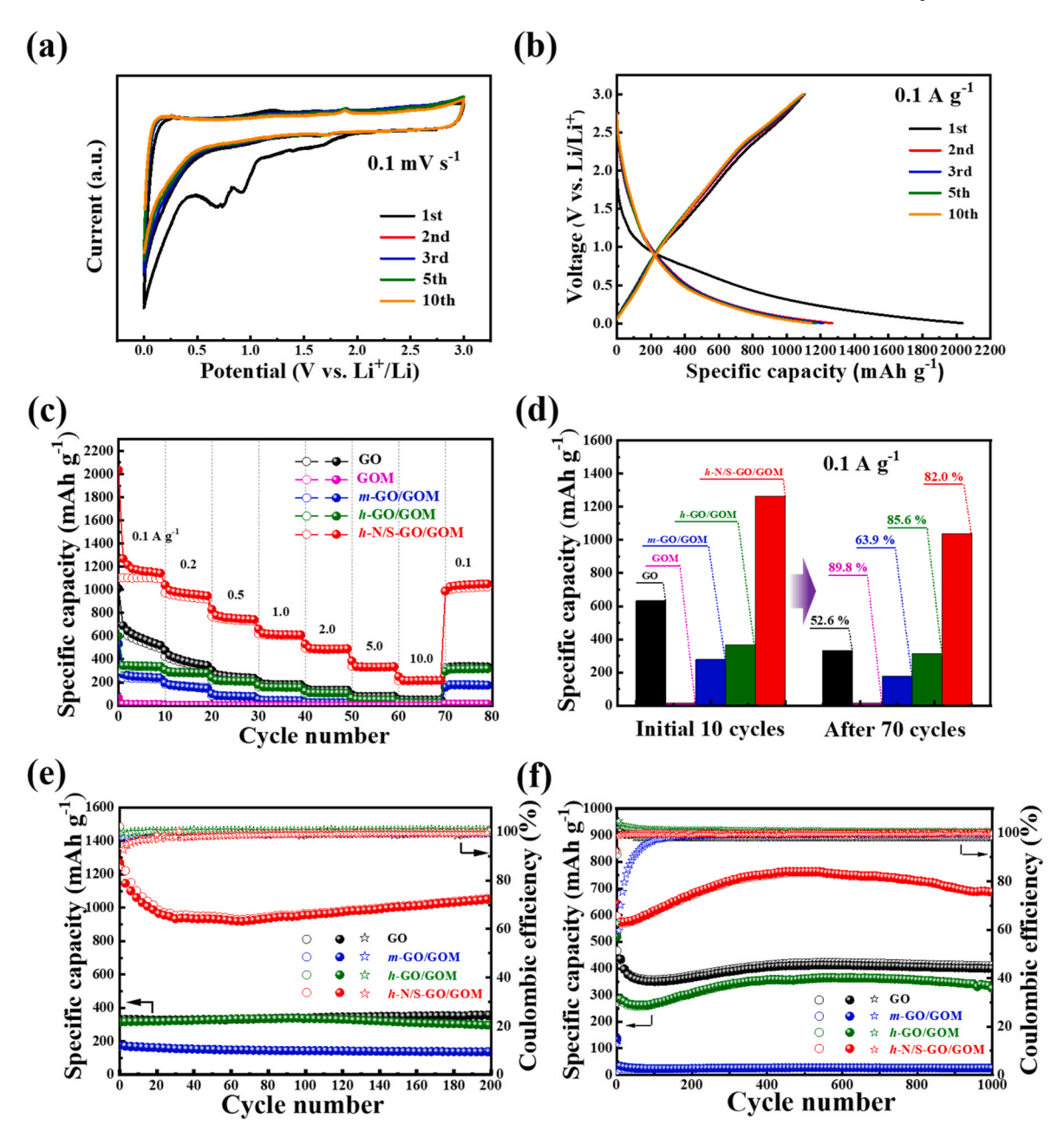


Fig. 5. (a) CV curves of the h-N/S-GO/GOM anode at a scan rate of 0.1 mV s $^{-1}$, (b) GCD profiles of the h-N/S-GO/GOM anode at 0.1 A g $^{-1}$, (c) Rate capabilities of the h-N/S-GO/GOM and comparative (GO, GOM, m-GO/GOM, and h-GO/GOM) anodes at different current densities (0.1–10.0 A g $^{-1}$), and (d) their capacity retention ratios. The cycling performances and Coulombic efficiencies of the h-N/S-GO/GOM and comparative (GO, m-GO/GOM, and h-GO/GOM) anodes at current densities of (e) 0.1 A g $^{-1}$ and (f) 1.0 A g $^{-1}$.

(139 mAh g $^{-1}$), and h-GO/GOM (297 mAh g $^{-1}$) anodes. Additionally, the h-N/S-GO/GOM anode demonstrated a gradual increase in reversible capacity during prolonged cycling, suggesting the promotion of active site growth through interactions between Li-ions and functional groups in the nanocomposite [1,5]. A cycling test at a high current density of 1.0 A g $^{-1}$ was conducted to evaluate the long-term stability of the h-N/S-GO/GOM and comparative anodes (Fig. 5f). Graphene-based composites exhibited good cycling stability across all anodes [57,58]. Specifically, the h-N/S-GO/GOM anode (688 mAh g $^{-1}$) exhibited remarkable capacity retention even after 1000 cycles, attributed to its well-developed interconnected conductive network. The gradual increase in capacity observed during cycling can be attributed to the improved accessibility of Li-ions to the inner structure of the N/S co-doped nanocomposite (h-N/S-GO/GOM) [26]. As cycling progresses, the ability of the anode material to accommodate Li-ions increases,

leading to enhanced performance. This effect has been frequently reported in previous studies on graphene-based materials, where capacity increases were associated with gradual electrochemical activation of N/S co-doped anode materials [59]. With repeated cycling, more active sites are exposed, and the internal structure becomes increasingly accessible, enabling greater Li-ion storage and improving overall capacity. Notably, the reversible capacity of the h-N/S-GO/GOM anode exceeded that of most previously reported rGO-based anode materials (Fig. S8) [60–71]. These results underscore the potential of the h-N/S-GO/GOM anode as a promising graphene-based material with high reversible capacity, exceptional rate performance, and excellent cycling stability.

To explain the enhanced electrochemical performance of the h-N/S-GO/GOM anode compared to the GO, GOM, m-GO/GOM, and h-GO/GOM anodes, EIS measurements were conducted before and after 200

cycles at a current density of 0.1 A g $^{-1}$ (Fig. 6a). The impedance data were fitted using equivalent electrical circuit models (inset images in Fig. 6a and b), with the fitting data listed in Table 2. Nyquist plots of the h-N/S-GO/GOM and comparative anodes before cycling showed a semicircle in the high-frequency region, corresponding to the solution resistance (R_s) and charge transfer resistance (R_c), and a straight line in the low-frequency region, indicating the Warburg resistance (Z_w) of the electrode (Fig. 6a) [70]. The h-N/S-GO/GOM anode exhibited lower R_s (2.60 Ω) and R_{ct} (20.97 Ω) values than the m-GO/GOM and h-GO/GOM anodes. Its hierarchical network structure facilitates charge transfer between the electrode and electrolyte, resulting in a shorter Li-ion diffusion path and more active sites, contributing to its superior electrical performance [5,22,69,72,73].

After 200 cycles, the h-N/S-GO/GOM anode exhibited two distinct semicircles in the EIS diagram. In contrast, comparison samples such as GO/GOM and GOM showed a merged semicircle in the EIS diagram, likely due to the high reactivity of organic components, rapid surface reactions, or complex interactions between the electrolyte and active material [74]. To address this, we applied an equivalent circuit model to separate the merged semicircle into two individual components, enabling a more detailed analysis of SEI formation and charge-transfer processes (Fig. S9). The first semicircle in the high-frequency region and the second semicircle in the middle-frequency region correspond to the resistances of the SEI layer (R_{sei}) and R_{ct} , respectively (Fig. 6b) [70]. In the *m*-GO/GOM and *h*-GO/GOM anodes, the R_{ct} values increased after cycling due to poor interfacial contact between the electrode materials [71]. Conversely, the cross-linked structure of the GO nanosheets and GOM in the h-N/S-GO/GOM anode induced a more stable and rigid SEI layer. The conjugated bonds formed a stable SEI film that minimized the surface area and stabilized the film [75]. Thus, the h-N/S-GO/GOM anode exhibited R_{sei} and R_{ct} values of 8.04 and 18.03 Ω , respectively, which were considerably lower than those of the m-GO/GOM and h-GO/GOM anodes. Additionally, the R_{ct} value at the interface between the electrode and electrolyte decreased after cycling, as the N/S co-doping provided more active sites. However, the Rs of the h-N/S-GO/GOM anode was 13.17 Ω after 200 cycles, which was higher than that of the other comparative anodes (Table 2). This suggests that the pore size decreased due to the formation of a stable SEI layer and abundant O-containing functional groups [76,77]. Moreover, the h-N/S-GO/GOM powder exhibited the highest electrical conductivity of $4.13 \times 10^{-6} \text{ S cm}^{-1}$ at a pressure of 100 kgf, consistent with the EIS results (Table 2).

FESEM images of the surface morphology of the $h\textsc{-}\mathrm{N/S}\textsc{-}\mathrm{GO/GOM}$ and

comparative (GO, m-GO/GOM, and h-GO/GOM) anodes before and after 200 cycles are shown in Fig. 7 and Fig. S10. After 200 lithiation/delithiation cycles, the h-N/S-GO/GOM anode, with its conjugated bonds and N/S co-doping, displayed a relatively smoother surface due to stable SEI growth, compared to the comparative anodes (Fig. 7f). In contrast, the GO, m-GO/GOM, and h-GO/GOM anodes exhibited highly rough topologies due to immiscibility and poor interface interactions, consistent with the EIS results (Fig. 7d and e, Fig. S10b). The balanced SEI layer growth on the electrode surface of the h-N/S-GO/GOM anode prevented structural cracking, contributing to its excellent and stable electrochemical performance [78].

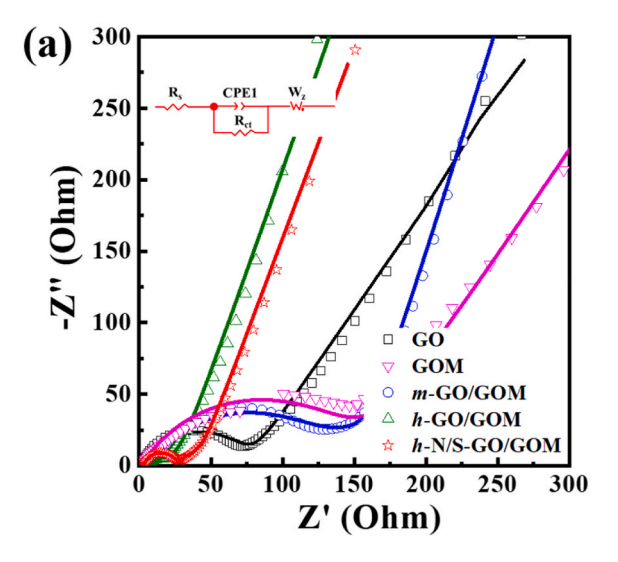
To further understand the superior electrochemical performance of the h-N/S-GO/GOM anode, its Li-ion storage kinetics were investigated using CV measurements. Fig. 8a displays the CV curves of the h-N/S-GO/GOM anode from 0.1 to 2.0 mV s⁻¹. As the scan rate increased, the CV curves maintained a similar shape, with the anodic peaks shifting slightly to higher potentials and the cathodic peaks shifting to lower potentials due to electrode polarization effects [79]. The degree of the capacitive effect can be qualitatively analyzed using the relationship between the measured current (i) and the scan rate (ν) from the CV curves [80].

$$i = av^b$$
 (2)

where a denotes an adjustable parameter, and b denotes the slope of the $\log(\nu)-\log(i)$ plot. The $\log(\nu)-\log(i)$ plots and b-values of the h-N/S-GO/GOM anode at various scan rates are shown in Fig. 8b. Energy storage modes can be classified into two types: diffusion-controlled and capacitance-controlled processes. A b-value close to 1.0 corresponds to an ideal capacitance-controlled process, while a b-value close to 0.5 indicates diffusion-controlled processes [70]. The b-values for the four peaks were calculated as 0.73 (I, 0.5 V), 0.79 (II, 1.0 V), 0.83 (III, 1.75 V), and 0.74 (IV, 2.0 V), respectively. Thus, all b-values represent capacitive charge-storage kinetics. To quantitatively determine the capacitive contribution, the current response i (V) at the corresponding potential was separated into capacitance- and diffusion-controlled contributions ($k_1\nu$ and $k_2\nu^{1/2}$, respectively) using the following equation [81]:

$$i(V) = k_1 v + k_2 v^{1/2}$$
(3)

The capacitive contribution ratios of GO, m-GO/GOM, h-GO/GOM, and h-N/S-GO/GOM anodes, obtained from their CV curves at scan rates from 0.1 to 2.0 mV s⁻¹ (Fig. 8a and S11), are shown in Fig. 8c, d, and



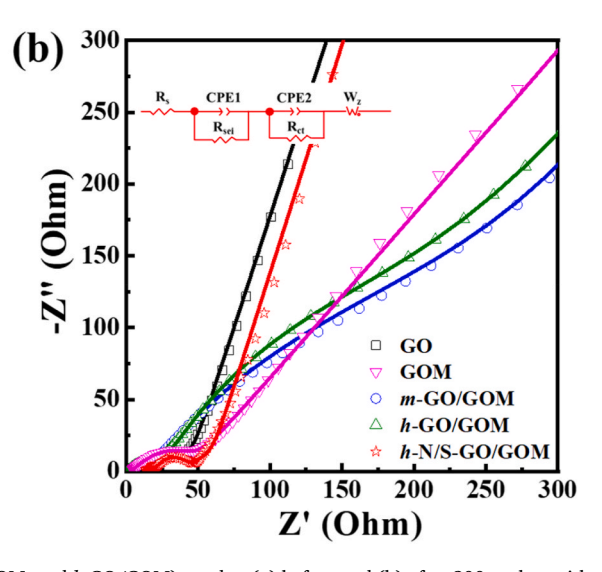


Fig. 6. Nyquist plots of the *h*-N/S-GO/GOM and comparative (GO, GOM, *m*-GO/GOM, and *h*-GO/GOM) anodes: (a) before and (b) after 200 cycles, with equivalent circuits shown in the insets.

Table 2Resistance values calculated from Nyquist plots for the *h*-N/S-GO/GOM and comparative (GO, GOM, *m*-GO/GOM, and *h*-GO/GOM) anodes. Electrical conductivity values of the *h*-N/S-GO/GOM and comparative (GO, GOM, *m*-GO/GOM) powders.

Samples	Solution re $R_s(\Omega)$	esistance,	Resistance $R_{\text{sei}}(\Omega)$	of SEI layer,	Charge transfer resistance, $R_{\rm ct} (\Omega)$		Electrical conductivity (S cm ⁻¹)
	Before	After 200 cycles	Before	After 200 cycles	Before	After 200 cycles	
GO	1.78	4.18	-	8.46	74.42	14.43	1.19×10^{-6}
GOM	1.83	3.70	_	15.88	151.60	24.19	3.45×10^{-6}
m-GO/GOM	5.52	2.24	_	16.19	118.90	266.60	1.73×10^{-6}
h-GO/GOM	2.91	1.38	_	25.57	26.41	137.60	3.75×10^{-6}
h-N/S-GO/GOM	2.60	13.17	-	8.04	20.97	18.03	4.13×10^{-6}

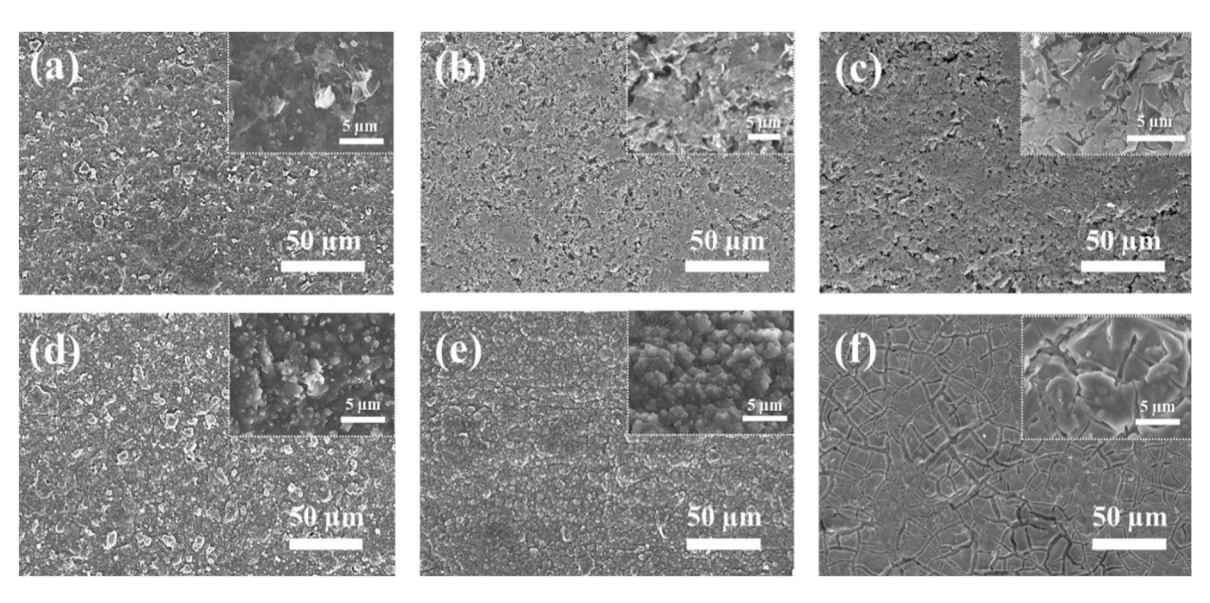


Fig. 7. FESEM images of (a, d) *m*-GO/GOM, (b, e) *h*-GO/GOM, and (c, f) *h*-N/S-GO/GOM anodes: (a–c) before and (d–f) after 200 cycles at a current density of 0.1 A g⁻¹ (high-magnification FESEM images are shown in the insets).

S12. The overall capacitive contributions at various scan rates were determined by calculating k_1 and K_2 . The h-N/S-GO/GOM anode exhibited a capacitive contribution of 95.7 % at 2.0 mV s⁻¹ (Fig. 8c). Moreover, the capacitive contribution increased from 83.3 % to 95.7 % as the scan rate increased (Fig. 8d). Notably, the GO anode, with abundant O-containing functional groups, primarily exhibited a surface capacitive behavior (94.1 % at 2.0 mV s⁻¹) (Fig. 8d and Fig. S12a). The m-GO/GOM anode displayed a slightly decreased capacitive contribution compared to the GO anode (90.5 % at 2.0 mV s⁻¹) (Fig. 8d and Fig. S12b). The h-GO/GOM anode showed a high level of diffusive contribution, which could be attributed to the more porous structure resulting from the additional hydrothermal process (Fig. 8d and Fig. S12c), as supported by the BET SSA results (Table 1). The h-N/S-GO/GOM anode exhibited a significantly enhanced capacitive contribution compared to the h-GO/GOM anode, due to N/S co-doping. The highest capacitive contribution ratio of the h-N/S-GO/GOM anode was attributed to its excellent electrical conductivity, stable surface chemistry, and improved redox reaction kinetics [80,81].

4. Conclusions

In this study, we successfully synthesized an all-carbonaceous graphene-based nanocomposite, *h*-N/S-GO/GOM, with a hierarchical interconnected network through a mild hydrothermal method incorporating GOM onto GO nanosheets. This process facilitated the generation of N/S co-doping and cross-linked bonding, effectively enhancing the interaction between hydrophilic GO and hydrophobic GOM in aqueous solution. The resulting nanocomposite exhibited rapid electron transfer, providing efficient charge transfer pathways, numerous active sites, and

Li-ion channels, leading to a high reversible specific capacity of 1050 mA h g-1 after 200 cycles at 0.1 A g-1. Furthermore, it demonstrated excellent rate capability, retaining a high capacity of 688 mA h g⁻¹ even after 1000 cycles at 1.0 A g⁻¹. The capacity increase in h-N/S-GO/GOM nanocomposites can be attributed to π - π bonding, which enhances the structural integrity of the nanocomposite and enables more efficient Liion diffusion. The hierarchical interconnected network, supported by π - π interactions and hydrogen bonding, resulted in the observed improvements in charge and ion transport within the h-N/S-GO/GOM nanocomposite. Thus, the outstanding Li storage performance of the $h\!\!-\!\!$ N/S-GO/GOM anode as a 2D graphene-based material enables high capacity at limited electrode densities. Overall, the h-N/S-GO/GOM anode presents a promising solution to the challenges associated with traditional graphite-based anodes, paving the way for the development of high-performance, environmentally friendly LIBs for various applications, including EVs and ESSs.

CRediT authorship contribution statement

Wooree Jang: Writing – original draft, Methodology, Investigation, Formal analysis, Data curation, Conceptualization. Jongmin Kim: Methodology, Investigation, Data curation. Seoyun Lee: Methodology, Investigation. Seokhoon Ahn: Methodology, Investigation, Conceptualization. Hyeyoung Koo: Supervision, Methodology, Investigation, Conceptualization. Cheol-Min Yang: Writing – review & editing, Supervision, Resources, Project administration, Methodology, Investigation, Funding acquisition, Conceptualization.

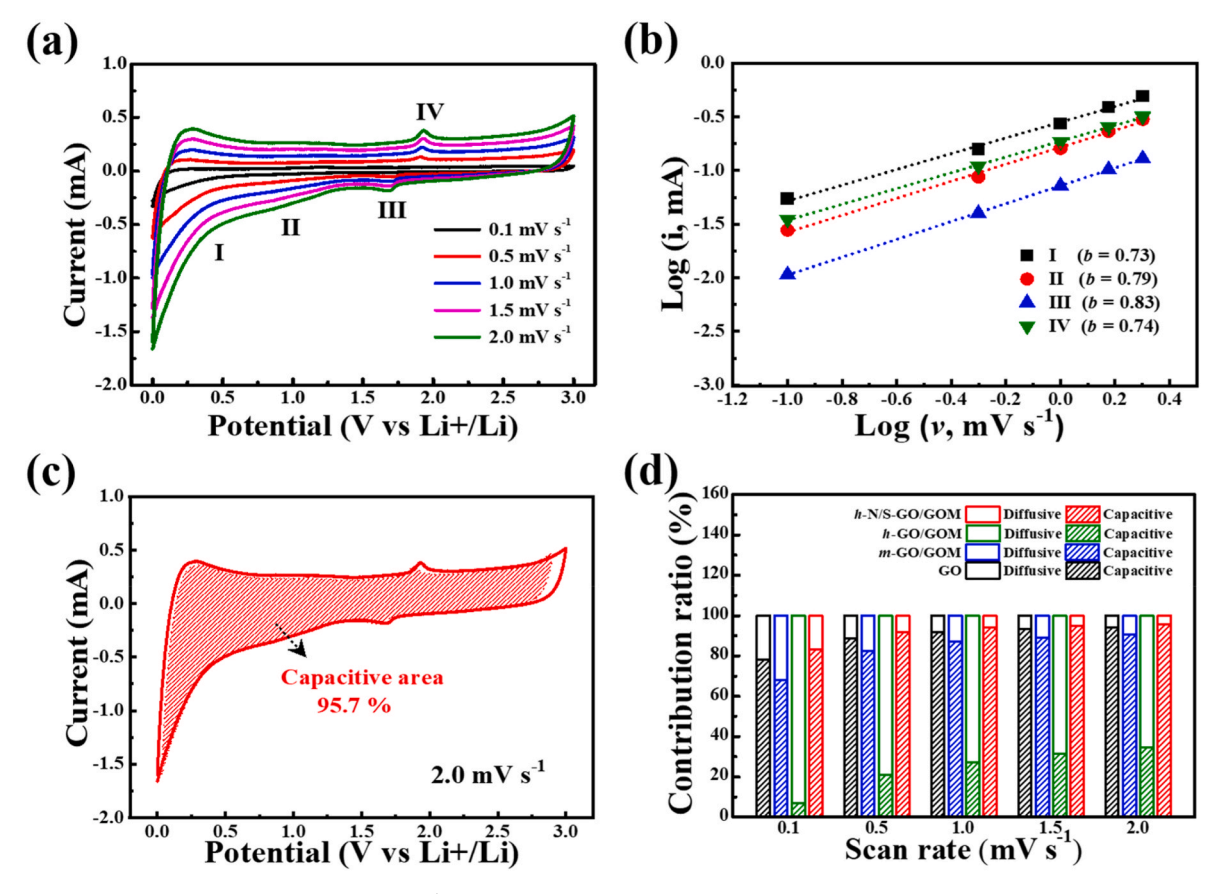


Fig. 8. (a) CV curves at different scan rates of $0.1-1.0 \text{ mV s}^{-1}$, (b) plots of log(scan rate) against log(peak current), (c) capacitive contribution in CV curve at 2.0 mV s^{-1} of the h-N/S-GO/GOM anode, and (d) capacitive and diffusive contribution ratios at different scan rates for the h-N/S-GO/GOM and comparative (GO, m-GO/GOM, and h-GO/GOM) anodes.

Declaration of competing interest

The authors declare that they have no known competing financial interests or personal relationships that could have appeared to influence the work reported in this paper.

Acknowledgements

This work was supported by the Korea Institute of Science and Technology (KIST) Institutional Program and the Commercialization Promotion Agency for R&D Outcomes (COMPA) grant funded by the Korean Government (Ministry of Science and ICT) (RS-2023-00304729).

Appendix A. Supplementary data

Supplementary data to this article can be found online at https://doi.org/10.1016/j.compositesb.2024.111994.

Data availability

Data will be made available on request.

References

- [1] Xu J, Mahmood J, Dou Y, Dou S, Li F, Dai L, Baek J-B. 2D Frameworks of C₂N and C₃N as new anode materials for lithium-ion batteries. Adv Mater 2017;29:1702007.
- [2] Kim SY, Kim CH, Yang C-M. Binder-free silicon anodes wrapped in multiple graphene shells for high-performance lithium-ion batteries. J Power Sources 2021; 486:229350.
- [3] Chen Y, Kang Y, Zhao Y, Wang L, Liu J, Li Y, Liang Z, He X, Li X, Tavajohi N, Li B. J Energy Chem 2021;59:83–9.

- [4] Zhang H, Yang Y, Ren D, Wang L, He X. Graphite as anode materials: fundamental mechanism, recent progress and advances. Energy Storage Mater 2021;36:147–70.
- [5] Park J, Lee CW, Joo SH, Park JH, Hwang C, Song H-K, Park YS, Kwak SK, Ahn S, Kang SJ. Contorted polycyclic aromatic hydrocarbon: promising Li insertion organic anode. J Mater Chem A 2018;6:12589–97.
- [6] Zhang C, Dong L, Zheng N, Zhu H, Wu C, Zhao F, Liu W. Aligned graphene array anodes with dendrite-free behavior for high-performance Li-ion batteries. Energy Storage Mater 2021;37:296–305.
- [7] Hossain MH, Chowdhury MA, Hossain N, Islam MA, Mobarak MH. Advances of lithium-ion batteries anode materials—A review. Chem Eng J Adv 2023;16:100569.
- [8] Khan BM, Oh WC, Nuengmatch P, Ullah K. Role of graphene-based nanocomposites as anode material for Lithium-ion batteries. Mater Sci Eng B 2023;287:116141.
- [9] Kim JH, Kim J, Jang W, Lee J, Yang C-M. Electrical bridging effects of dual-carbon microsphere frameworks in Si-based composite anodes for high-performance Li-ion batteries. Appl Surf Sci 2023;641:158494.
- [10] Li N, Sun L, Wang K, Xu S, Zhang J, Guo X, Liu X. Sandwiched N-carbon@Co₉S₈@ Graphene nanosheets as high capacity anode for both half and full lithium-ion batteries. J Energy Chem 2020;51:62–71.
- [11] Jo AH, Kim SY, Kim JH, Kim YA, Yang C-M. Robust core-shell carbon-coated silicon-based composite anode with electrically interconnected spherical framework for lithium-ion battery. Int J Energy Res 2023;2023:6874429.
- [12] Li Y, Fu Y, Chen S, Huang Z, Wang L, Song Y. Porous Fe₂O₃/Fe₃O₄@Carbon octahedron arrayed on three-dimensional graphene foam for lithium-ion battery. Compos B Eng 2019;171:130–7.
- [13] Wang S, Yang B. Dirac nodal line semimetal of three-dimensional cross-linked graphene network as anode materials for Li-ion battery beyond graphite. ACS Appl Energy Mater 2021;4:2091–7.
- [14] Zhao H, Zeng X, Zheng T, Liu S, Yang J, Hao R, Li F. Three-dimensional porous aerogel assembly from ultrathin rGO@SnO₂ nanosheets for advanced lithium-ion batteries. Compos B Eng 2022;231:109591.
- [15] Yu S, Guo B, Zeng T, Qu H, Yang J. Graphene-based lithium-ion battery anode materials manufactured by mechanochemical ball milling process: a review and perspective. Compos B Eng 2022;246:110232.
- [16] Wang J, Tee K, Lee Y, Riduan SN, Zhang Y. Hexaazatriphenylene derivatives/GO composites as organic cathodes for lithium ion batteries. J Mater Chem A 2018;6: 2752–7
- [17] Sieuw L, Jouhara A, Quarez E, Auger C, Gohy J-F, Poizot P, Vlad A. A H-bond stabilized quinone electrode material for Li-organic batteries: the strength of weak bonds. Chem Sci 2019;10:418–26.

[18] Han C, Li H, Shi R, Zhang T, Tong J, Li J, Li B. Organic quinones towards advanced electrochemical energy storage: recent advances and challenges. J Mater Chem A 2019;7:23378–415.

- [19] Wang Y, Deng Y, Qu Q, Zheng X, Zhang J, Liu G, Battaglia VS, Zheng H. Ultrahigh-capacity organic anode with high-rate capability and long cycle life for lithium-ion batteries. ACS Energy Lett 2017;2:2140–8.
- [20] Park J, Lee CW, Park JH, Joo SH, Kwak SK, Ahn S, Kang SJ. Capacitive organic anode based on fluorinated-contorted hexabenzocoronene: applicable to lithiumion and sodium-ion storage cells. Adv Sci 2018;5:1801365.
- [21] Chen X, Yin X, Aslam J, Sun W, Wang Y. Recent progress and design principles for rechargeable lithium organic batteries. Electrochem Energy Rev 2022;5:1–32.
- [22] Zhu D, Yuan J, Wang T, Dai Y, Peng Y, Li W, Li A, Zhang J. A novel one-step method to prepare N, S Co-doped sub-fluorinated carbon electrode materials for ultrahigh-rate lithium-fluorinated carbon battery. J Power Sources 2022;551: 232188.
- [23] Appavu B, Thiripuranthagan S. Visible active N, S co-doped TiO₂/graphene photocatalysts for the degradation of hazardous dyes. J Photochem Photobiol, A 2017;340:146–56.
- [24] Xiong J, Pan Q, Zheng F, Xiong X, Yang C, Hu D, Huang C. N/S co-doped carbon derived from cotton as high performance anode materials for lithium ion batteries. Front Chem 2018;6:78.
- [25] Cheng X, Ran F, Huang Y, Zheng R, Yu H, Shu J, Xie Y, He Y-B. Insight into the synergistic effect of N, S co-doping for carbon coating layer on niobium oxide anodes with ultra-long life. Adv Funct Mater 2021;31:2100311.
- [26] Cai D, Lv X, Tian W, Hu Z, Ma K, Tan S, Ji J, Wang C, Shi C, Tan N. Facile synthesis of N and S co-doped graphene sheets as anode materials for high-performance lithium-ion batteries. J Alloys Compd 2018;731:235–42.
- [27] Zhang H. One-pot fabrication of N, S co-doped carbon with 3D hierarchically porous frameworks and high electron/ion transfer rate for lithium-ion batteries. Chem Eng Sci 2021;234:116453.
- [28] Ren J-T, Wan C-Y, Pei T-Y, Lv X-W, Yuan Z-Y. Promotion of electrocatalytic nitrogen reduction reaction on N-doped porous carbon with secondary heteroatoms. Appl Catal B Environ 2020;266:118633.
- [29] Kumar V. Urea/thiourea based optical sensors for toxic analytes: a convenient path for detection of first nerve agent (tabun). Bull Chem Soc Jpn 2021;94:309–26.
- [30] Qian H-L, Zhu M-S, Du M-L, Ran X-Q, Yan X-P. Engineering linkage as functional moiety into irreversible thiourea-linked covalent organic framework for ultrafast adsorption of Hg(II). J Hazard Mater 2022;427:128156.
- [31] Custelcean R. Crystal engineering with urea and thiourea hydrogen-bonding groups. Chem Commun 2008;3:295–307.
- [32] Zhao K, Zhang T, Chang H, Yang Y, Xiao P, Zhang H, Li C, Tiwary CS, Ajayan PM, Chen Y. Super-elasticity of three-dimensionally cross-linked graphene materials all the way to deep cryogenic temperatures. Sci Adv 2019;5:eaav2589.
- [33] Qin Y, Jiang Z, Guo L, Huang J, Jiang Z-J, Liu M. Sulfurization synthesis of a new anode material for Li-ion batteries: understanding the role of sulfurization in lithium ion conversion reactions and promoting lithium storage performance. J Mater Chem A 2019;7:21270–9.
- [34] Kim JH, Ko Y, Kim YA, Kim KS, Yang C-M. Sulfur-doped carbon nanotubes as a conducting agent in supercapacitor electrodes. J Alloys Compd 2021;855:157282.
- [35] Tian Z, Li J, Zhu G, Lu J, Wang Y, Shi Z, Xu C. Facile synthesis of highly conductive sulfur-doped reduced graphene oxide sheets. Phys Chem Chem Phys 2016;18: 1125–30.
- [36] Sharma R, Chadha N, Saini P. Determination of defect density, crystallite size and number of graphene layers in graphene analogues using X-ray diffraction and Raman spectroscopy. Indian J Pure Appl Phys 2017;55:625–9.
- [37] Botas C, Alvarez P, Blanco C, Santamaria R, Cranda M, Gutierrez MD, Rodriguez-Reinoso F, Menendez R. Critical temperatures in the synthesis of graphene-like materials by thermal exfoliation-reduction of graphite oxide. Carbon 2013;52: 476–85.
- [38] Johra FT, Jung W-G. Hydrothermally reduced graphene oxide as a supercapacitor. Appl Surf Sci 2015;357:1911–4.
- [39] Xia B, Wang Z, Wang T, Chen S, Wu H, Zhang B, Si Y, Chen Z, Li B-W, Kou Z, He D. Bridging sheet size controls densification of MXene films for robust electromagnetic interference shielding. iScience 2022;25:105001.
- [40] Kumar K, Kumar U, Singh M, Yadav BC. Synthesis and characterizations of exohedral functionalized graphene oxide with iron nanoparticles for humidity detection. J Mater Sci Mater Electron 2019;30:13013–23.
- [41] Singh PK, Singh PK, Sharma K. Electrochemical synthesis and characterization of thermally reduced graphene oxide: influence of thermal annealing on microstructural features. Mater Today Commun 2022;32:103950.
- [42] Kim J, Jo Y, Ahmed ATA, Inamdar AI, Cho S, Kim H, Im H. Density-modulated multilayered homo-junction tungsten oxide anode materials for high-capacity Liion batteries with long-term stability. Int J Energy Res 2022;46:1387–97.
- [43] Mehner T, Uland M, Lampke T. Analytical model to calculate the grain size of bulk material based on its electrical resistance. Metals 2021;11:21.
- [44] Kudin KN, Ozbas B, Schniepp HC, Prud'homme RK, Aksay IA, Car R. Raman spectra of graphite oxide and functionalized graphene sheets. Nano Lett 2008;8: 36–41.
- [45] Papageorgiou DG, Kinloch IA, Young RJ. Mechanical properties of graphene and graphene-based nanocomposites. Prog Mater Sci 2017;90:75–127.
- [46] Hwang H, Kim CH, Wee J-H, Han JH, Yang C-M. High-density graphene/single-walled carbon nanohorn composite supercapacitor electrode with high volumetric capacitance. Appl Surf Sci 2019;489:708–16.
- [47] Childres I, Jauregui LA, Park W, Cao H, Chen YP. Raman spectroscopy of graphene and related materials. New Dev Phot Mater Res 2013;1:1–20.

[48] Yoshio M, Wang H, Fukuda K, Hara Y, Adachi Y. Effect of carbon coating on electrochemical performance of treated natural graphite as lithium-ion battery anode material. J Electrochem Soc 2000;147:1245–50.

- [49] Yan Z, Hu Q, Yan G, Li H, Shih K, Yang Z, Li X, Wang Z, Wang J. Co₃O₄/Co nanoparticles enclosed graphitic carbon as anode material for high performance Liion batteries. Chem Eng J 2017;321:495–501.
- [50] Ma X, Ning G, Sun Y, Pu Y, Gao J. High capacity Li storage in sulfur and nitrogen dual-doped graphene networks. Carbon 2014;79:310–20.
- [51] Guo R, Wang Y, Heng S, Zhu G, Battaglia VS, Zheng H. Pyromellitic dianhydride: a new organic anode of high electrochemical performances for lithium ion batteries. J Power Sources 2019;436:226848.
- [52] He S, Shen Z, Yu J, Guan H, Lu G, Xiao T, Yang S, Zou Y, Bu L. Vertical miscibility of bulk heterojunction films contributes to high photovoltaic performance. Adv Mater Interfac 2020;7:2000577.
- [53] Xie Z, Li X, Li W, Chen M, Qu M. Graphene oxide/lithium titanate composite with binder-free as high capacity anode material for lithium-ion batteries. J Power Sources 2015;273:754–60.
- [54] Xie J, Zhang Q. Recent progress in rechargeable lithium batteries with organic materials as promising electrodes. J Mater Chem A 2016;4:7091–106.
- [55] Zhang C, He Y, Mu P, Wang X, He Q, Chen Y, Zeng J, Wang F, Xu Y, Jiang JX. Toward high performance thiophene-containing conjugated microporous polymer anodes for lithium-ion batteries through structure design. Adv Funct Mater 2018; 28:1705432.
- [56] Xie Z, Yu Z, Fan W, Peng G, Qu M. Effects of functional groups of graphene oxide on the electrochemical performance of lithium-ion batteries. RSC Adv 2015;5: 90041–8
- [57] Deng L, Wei T, Liu J, Zhan L, Chen W, Cao J. Recent developments of carbon-based anode materials for flexible lithium-ion batteries. Crystals 2022;12:1279.
- [58] Zhou L, Yang H, Han T, Song Y, Yang G, Li L. Carbon-based modification materials for lithium-ion battery cathodes: advances and perspectives. Front Chem 2022;10: 914930.
- [59] Ai W, Luo Z, Jiang J, Zhu J, Du Z, Fan Z, Xie L, Zhang H, Huang W, Yu T. Nitrogen and sulfur codoped graphene: multifunctional electrode materials for highperformance Li-ion batteries and oxygen reduction reaction. Adv Mater 2014;26: 6186–92.
- [60] Jang J, Ki H, Kang Y, Son M, Auxilia FM, Seo H, Kim I-H, Kim K-H, Park K-H, Kim Y, Kim WB, Ham M-H, Kim IS. Chemically prelithiated graphene for anodes of Li-ion batteries. Energy Fuels 2020;34:13048–55.
- [61] Lian P, Zhu X, Liang S, Li Z, Yang W, Wang H. Large reversible capacity of high quality graphene sheets as an anode material for lithium-ion batteries. Electrochim Acta 2010;55:3909–14.
- [62] Wu ZS, Ren W, Xu L, Li F, Cheng HM. Doped graphene sheets as anode materials with superhigh rate and large capacity for lithium ion batteries. ACS Nano 2011;5: 5463–71.
- [63] Xiang HF, Li ZD, Xie K, Jiang JZ, Chen JJ, Lian PC, Wu JS, Yu Y, Wang HH. Graphene sheets as anode materials for Li-ion batteries: preparation, structure, electrochemical properties and mechanism for lithium storage. RSC Adv 2012;2: 6792-9
- [64] Fu C, Zhao G, Zhang H, Li S. Evaluation and characterization of reduced graphene oxide nanosheets as anode materials for lithium-ion batteries. Int J Electrochem Sci 2013;8:6269–80.
- [65] Zhang X, Han S, Xiao P, Fan C, Zhang W. Thermal reduction of graphene oxide mixed with hard carbon and their high performance as lithium ion battery anode. Carbon 2016;100:600–7.
- [66] Ding X, Lei S, Du C, Xie Z, Li J, Huang X. Small-sized CuS nanoparticles/N, S codoped rGO composites as the anode materials for high-performance lithium-ion batteries. Adv Mater Interfac 2019;6:1900038.
- [67] Huang Q, Hu J, Wen S, Zhang X, Liu G, Chang S, Liu Y. Sulfur-doped and bio-resinderived hard Carbon@rGO composites as sustainable anodes for lithium-ion batteries. Front Chem 2020;8:241.
- [68] Luan Y, Yin J, Zhu K, Cheng K, Yan J, Ye K, Wang G, Cao D. Arc-discharge production of high-quality fluorine-modified graphene as anode for Li-ion battery. Chem Eng J 2020;392:123668.
- [69] Du Z, Ai W, Xie L, Huang W. Organic radical functionalized graphene as a superior anode material for lithium-ion batteries. J Mater Chem A 2014;2:9164–8.
- [70] Kim J, Jang W, Kim JH, Yang C-M. Synthesis of graphene quantum dots-coated hierarchical CuO microspheres composite for use as binder-free anode for lithiumion batteries. Compos B Eng 2021;222:109083.
- [71] Yu F, Zhao L, Zhang H, Sun Z, Li Y, Hu Q, Chen Y. Cathode/gel polymer electrolyte integration design based on continuous composition and preparation technique for high performance lithium ion batteries. RSC Adv 2021;11:3854–62.
- [72] Wasalathilake KC, Li H, Xu L, Yan C. Recent advances in graphene based materials as anode materials in sodium-ion batteries. J Energy Chem 2020;42:91–107.
- [73] Tang M, Zhu S, Liu Z, Jiang C, Wu Y, Li H, Wang B, Wang E, Ma J, Wang C. Tailoring π-conjugated systems: from π-π stacking to high-rate-performance organic cathodes. Chem 2018;4:2600–14.
- [74] Wildfeuer L, Gieler P, Karger A. Combining the distribution of relaxation times from EIS and time-domain data for Parameterizing equivalent circuit models of lithium-ion batteries. Batteries 2021;7:52.
- [75] Li C-Y, Wu M-S, Chen W-R, Wang Q-Y, Rong Y-J, Zhang X-P. A π-conjugated dualfunctional redox mediator facilitates the construction of dendrite-free lithiumoxygen batteries. J Mater Chem A 2023;11:937–42.
- [76] Xu A, Weng Y, Zhao R. Permeability and equivalent circuit model of ionically conductive mortar using electrochemical workstation. Materials 2020;13:1179.
- [77] Watanabe Y, Kinoshita S, Wada S, Hoshino K, Morimoto H, Tobishima S. Electrochemical properties and lithium ion solvation behavior of sulfone-ester

- mixed electrolytes for high-voltage rechargeable lithium cells. J Power Sources 2008;179:770–9.
- [78] Cho MK, You SJ, Woo JG, An J-C, Kang S, Lee H-W, Kim JH, Yang C-M, Kim YJ. Anomalous Si-based composite anode design by densification and coating strategies for practical applications in Li-ion batteries. Compos B Eng 2021;215: 108799.
- [79] Wan S, Liu X, Fu L, Zhou C, Chen H, Li G, Cao S, Liu Q. Hierarchical self-assembled SnS@ NS dual-doped carbon microflower spheres as anode for high performance lithium-ion batteries. J Alloys Compd 2021;870:159407.
- [80] Wang S, Cao F, Li Y, Zhang Z, Zhou D, Yang Y, Tang Z. MoS₂-coupled carbon nanosheets encapsulated on sodium titanate nanowires as super-durable anode material for sodium-ion batteries. Adv Sci 2019;6:1900028.
- [81] Wang Y, Kong D, Huang S, Shi Y, Ding M, Lim YV, Xu T, Chen F, Li X, Yang HY. 3D carbon foam-supported WS₂ nanosheets for cable-shaped flexible sodium ion batteries. J Mater Chem A 2018;6:10813.